Linear High-Resolution BioMEMS Force Sensors With Large Measurement Range

Jagannathan Rajagopalan, Alireza Tofangchi, and M. Taher A. Saif

***Abstract*—We present a set of displacement-based high-resolution (50 pN) micromechanical force sensors with a large force measurement range (1 μN). Typically, force sensors that have high resolution have a limited force measurement range and vice versa. The force sensors presented here overcome this limitation and, in addition, have a highly linear force–displacement response. The sensors (≈ 3 mm $\times$ 4 mm $\times$ 150 μm) are composed of a series of flexible beams attached to a rigid probe that deform when subjected to an external force. The force is obtained by optically measuring the displacement of the probe with respect to a fixed reference beam. The force sensors are fabricated using a simple two-mask process that allows for their stiffness to be varied over a wide range. Furthermore, we have developed a novel scheme to avoid capillary forces during the immersion and removal of these sensors from aqueous environments, which makes them highly suited for biological studies. We illustrate the capability and versatility of these sensors by measuring the *in vivo* force-deformation response of axons in *Drosophila melanogaster* (fruit fly). [2009-0327]**

***Index Terms*—Capillary forces, cell mechanics, force sensor, microelectromechanical systems.**

I. Introduction

In RECENT years, it has become increasingly evident that cell-generated forces play an important role in many physiological processes [1], [2]. Living cells respond to mechanical stimuli from their microenvironment both mechanically and biochemically [3]–[7]. Our understanding of how cells sense, apply, and respond to mechanical forces has been greatly aided by the development of a variety of new techniques [8]. These techniques fall broadly into two categories. The first class of techniques are used to study the mechanical behavior of entire cell populations, most commonly by imposing deformation through the substrate [9], [10] on which the cells are cultured. The second class of techniques are oriented toward studying the mechanical response of single cells and molecules. These include optical and magnetic tweezers [11], atomic force microscopes (AFMs) [12], optical stretchers [13], and magnetic twisting cytometry (MTC) [14]. Some techniques such as microfabricated postarray detector [15] and embedded particle tracking [16] have been used for both single-cell and cell-population studies. In addition to the aforementioned techniques, several microelectromechanical systems (MEMS)-based techniques have been developed recently for biological force measurements, the examples of which include piezoresistive cantilevers [17] and MEMS capacitive sensors [18], [19].

Single-cell techniques such as MTC and optical tweezers often have high force and displacement resolution but can induce only small cell deformations (on the order of 1 μm) and measure small forces (10 nN or less). AFMs are also usually used to measure small forces, although much larger forces (in the millinewton range) can be measured by using stiff cantilevers but with a lower resolution. However, large cell deformations are physiologically relevant [20], [21], and to study cell response in such cases, a set of mechanical sensors based on microfabrication technologies was developed [22], [23]. These microfabricated sensors used flexible beams to sense forces up to 1 μN and used a simple displacement-based force-sensing method that precluded the need for complex electronics/optics. However, these force sensors had lower force resolution (≈ 0.5 nN), and the force–displacement response was linear only over a limited displacement range (< 50 μm). In this paper, we present a new class of micromechanical sensors that significantly improves the resolution (50 pN) while preserving the range of force measurement of the aforementioned sensors. In addition, the new sensors have highly linear force–displacement response over the entire range of measurement and are fabricated using a simple two-mask process that substantially reduces the complexity of fabrication.

An essential requirement for micromechanical force sensors to be used in biological studies is the ability to operate in aqueous environments. This is a major challenge since the sensors have to withstand the extremely large forces required to break the meniscus during their immersion and removal from water. These capillary forces can cause severe structural damage to the sensors and compromise their functionality. To circumvent this problem, we have developed a novel scheme to insulate our force sensors from capillary forces during their immersion and removal from aqueous environments. We demonstrate the suitability of these sensors for biological applications by measuring the force-deformation response of axons in embryonic fruit flies (*Drosophila melanogaster*) *in vivo*.

II. Design of the Force Sensors

The force sensors are composed of a system of identical flexible beams attached to a rigid probe and a fixed beam that

Manuscript received December 22, 2009; revised July 30, 2010; accepted August 20, 2010. Date of publication October 11, 2010; date of current version November 30, 2010. This work was supported in part by the National Institutes of Health under Grant NIH/NINDS NS063405-01 and in part by the National Science Foundation under Grants NSF ECS 05-24675, NSF CMMI 0800870, and NSF ECCS 0801928. Subject Editor G. K. Fedder.

The authors are with the Department of Mechanical Science and Engineering, University of Illinois at Urbana–Champaign, Urbana, IL 61801-2906 USA (e-mail: saif@illinois.edu).

Color versions of one or more of the figures in this paper are available online at http://ieeexplore.ieee.org.

Digital Object Identifier 10.1109/JMEMS.2010.2076780

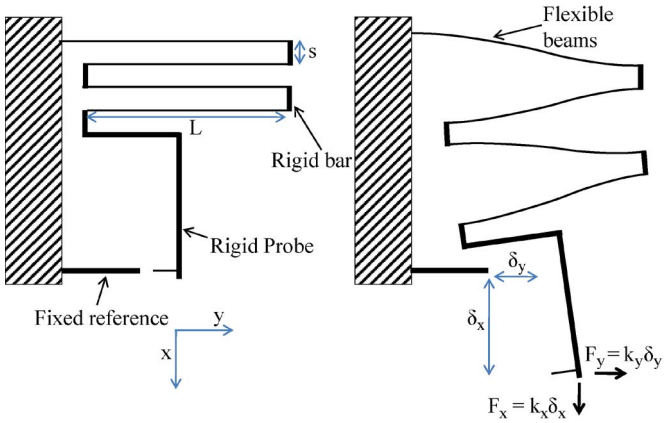

Fig. 1. Schematic of the force sensor. Because the flexible beams are connected in series, the deflection of the individual beams is small even when the overall deflection is large. This leads to high force resolution, as well as large linear force–displacement range.

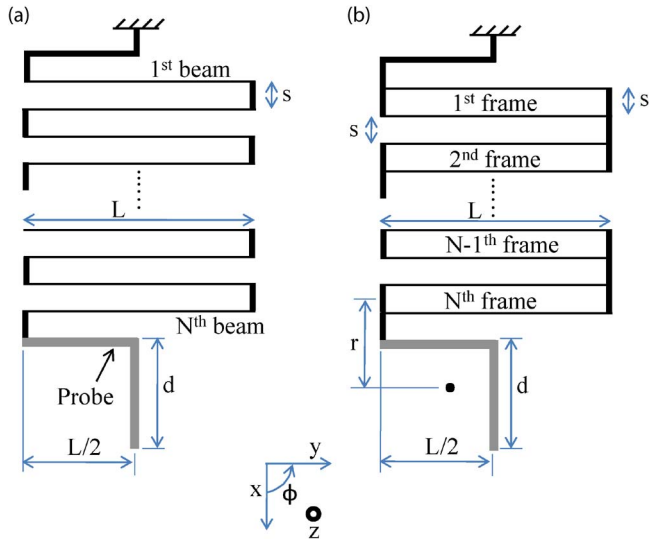

Fig. 2. Two configurations of beams considered for the force sensors. (a) Configuration I, where the basic repeating element is a single flexible beam. The probe is indicated in gray color. (b) Configuration II, where the repeating element is a frame. The black dot represents the center of mass of the probe. In both configurations, all the elements except the flexible beams are assumed to be rigid.

serves as a reference for displacement measurement (Fig. 1). The principle of operation of the force sensor is as follows. When subjected to an external force, the beams deform, and their total deflection is found by optically measuring the relative displacement of the probe with respect to the fixed reference beam. The external force is then given by the total deflection of the beams multiplied by their combined stiffness. The combined stiffness of the beams is calculated from their geometry and independently verified by calibration. Because of the use of optical measurement, only in-plane deflection of the beams can be measured in this setup.

As evident from Fig. 1, the beams are connected in series, and therefore, their combined stiffness is $1/N$ times the stiffness of each beam, where N is the total number of beams. As a result, the sensor can have high force resolution even if the stiffness of the individual beams is not very low. In addition, the resolution of the force sensors can be altered simply by varying N without changing the dimensions of the beams. More importantly, this design leads to a highly linear force–displacement relationship for the sensor. This is so because, even when the overall deflection (δ) is large, the deflection of the individual beams is still small, and hence, nonlinear effects are negligible.

For the thin rectangular beams used in these force sensors, bending and torsion are the primary modes of deformation since the axial stiffness is comparatively very large. For a beam of given dimensions, the bending and torsional stiffness depend on the boundary conditions, which, in turn, are determined by the configuration of the beams.

We considered two different configurations of beams for our force sensors. In configuration I [Fig. 2(a)], the basic repeating unit is a single flexible beam. The single beams are connected together by thick rigid beams to form a serpentine structure. In configuration II [Fig. 2(b)], a pair of flexible beams is connected by a rigid beam to form a frame. The frames are then connected together by rigid beams to form a serpentine structure. In this configuration, the frames are the basic repeating units as opposed to single beams. The two configurations have different sensitivities to forces in different directions as shown in the following. Note that, in these sensors, only the x and y deflections of the probe are measured optically.

A. Analysis of Force Sensor Configuration I

In this section, we analyze the deflection of the probe in the x- and y-directions (δ_{xp} and δ_{yp}) when it is subjected to forces F_x and F_y. To compute the deflection of the probe, we adopt the following notation: ϕ_i and δ_{xi} and δ_{yi} are the in-plane rotation and x and y displacements of beam i with respect to beam $i-1$, respectively. In the following derivations, we assume that ϕ_i, δ_{xi}, and δ_{yi} are small. We calculate the displacements of the probe due to F_x and F_y separately and use superposition principle to compute the total displacement.

1) Probe Deflection Due to F_x: The force F_x on the probe results in a moment $M = -F_x L/2$ and a force F_x at the end in each beam [Fig. 2(a)]. Therefore, the in-plane rotation of beam i with respect to beam $i-1$ is

$$\phi_i = \frac{F_x L^2}{2EI} + \frac{ML}{EI} = 0. \tag{1}$$

Here, $I = b^3 h/12$, and E is the Young's modulus. Our force sensors are made of single-crystal silicon, and the beams are oriented along the [110]-direction for which $E \approx 170$ GPa [24], [25]. b, h, and L are the thickness, depth, and length of the beams, respectively. In these sensors, typically, $b = 2-4$ μm, $h = 10-40$ μm, $L = 2-3$ mm, $d = 0.3-0.4$ mm, $s = 32-34$ μm, and $N = 8-24$ (see Fig. 2 for the definition of s and d). Since there is no rotation of the beams, the displacement of beam i with respect to beam $i-1$ is simply given by the deflection due to bending. Hence, $\delta_{xi} = F_x L^3/12EI$. The deflection of the probe is therefore

$$\delta_{xp} = \sum_{i=1}^{N} \delta_{xi} = \frac{NF_x L^3}{12EI}. \tag{2}$$

F_x does not cause any displacement of the beams in the y-direction. Therefore, $\delta_{yp} = 0$.

2) Probe Deflection Due to F_y: The force F_y on the probe results in an axial force F_y and a moment on each beam. Since the axial stiffness of the beam is very large compared to the bending stiffness, the effect of the axial force can be neglected. The moment on beam i due to F_y is

$$M_i = F_y\left((N+1-i)s+d\right). \tag{3}$$

The rotation of beam i with respect to beam $i-1$ is

$$\phi_i = \frac{M_i L}{EI}. \tag{4}$$

We first consider the deflection of the probe in the x-direction (δ_{xp}) due to the moment caused by F_y. The x displacement of beam i with respect to beam $i-1$ is

$$\delta_{xi} = (-1)^i L\sin\left(\sum_{j=1}^{i-1}\phi_j\right) + (-1)^i\frac{M_i L^2}{2EI}\cos\left(\sum_{j=1}^{i-1}\phi_j\right) - s\left(1-\cos\left(\sum_{j=1}^{i-1}\phi_j\right)\right). \tag{5}$$

The first and third terms in (5) correspond to the displacement caused by the rigid body rotation of beam i and the bar of length s that connects the beams. The second term corresponds to the deflection of beam i due to bending. The $(-1)^i$ factor arises because the contribution of the first two terms is positive for even-numbered beams and negative for odd-numbered beams. The x displacement of the probe is therefore given by

$$\delta_{xp} = \sum_{i=1}^{N}\delta_{xi} + (-1)^{(N+1)}\frac{L}{2}\sin\left(\sum_{i=1}^{N}\phi_i\right) - s\left(1-\cos\left(\sum_{i=1}^{N}\phi_i\right)\right). \tag{6}$$

The second and third terms in (6) correspond to the displacement caused by the rigid body rotation of the probe and the bar that connects the probe to the last beam. Since we assume small displacements and rotations, $\sin(\sum\phi_i)\approx\sum\phi_i$, and $\cos(\sum\phi_i)\approx 1$. Using these approximations in (5), we find

$$\sum_{i=1}^{N}\delta_{xi} = (-1)^N\frac{F_y L^2}{4EI}N\left((N+1)s+2d\right). \tag{7}$$

From (3) and (4)

$$\sum_{i=1}^{N}\phi_i = \frac{F_y L}{2EI}N\left((N+1)s+2d\right). \tag{8}$$

Therefore, we get from (6)

$$\delta_{xp} = \sum_{i=1}^{N}\delta_{xi} + (-1)^{(N+1)}\frac{L}{2}\sum_{i=1}^{N}\phi_i = 0. \tag{9}$$

In other words, F_y does not contribute to the x-direction displacement of the probe.

We now consider the displacement of the probe in the y-direction (δ_{yp}) due to the moment caused by F_y. The y displacement of beam i with respect to beam $i-1$ is

$$\delta_{yi} = (-1)^i\left[L\left(1-\cos\left(\sum_{j=1}^{i-1}\phi_j\right)\right) + \frac{M_i L^2}{2EI}\sin\left(\sum_{j=1}^{i-1}\phi_j\right)\right] + s\sin\left(\sum_{j=1}^{i-1}\phi_j\right). \tag{10}$$

Again, the first and third terms in (10) correspond to the displacement caused by the rotation of beam i and the bar that connects the beams. The second term corresponds to the deflection caused by bending. The y displacement of the probe is therefore given by

$$\delta_{yp} = \sum_{i=1}^{N}\delta_{yi} + (d+s)\sin\left(\sum_{i=1}^{N}\phi_i\right). \tag{11}$$

The second term in (11) corresponds to the displacement caused by the rotation of the probe and the bar that connects the probe to the last beam. Since only small displacements and rotations are considered, (10) reduces to

$$\delta_{yi} = \left[(-1)^i\frac{M_i L^2}{2EI} + s\right]\left(\sum_{j=1}^{i-1}\phi_j\right) \approx s\left(\sum_{j=1}^{i-1}\phi_j\right). \tag{12}$$

Note that, in (12), we have assumed $M_i L^2/2EI$, which is the deflection of beam i due to bending, to be small compared to s. In other words, only the rigid body rotation of the connecting bar contributes to δ_{yi}. Using (8), (11), and (12), the displacement of the probe in the y-direction is given by

$$\delta_{yp} = \frac{F_y LN}{6EI}\left[(2N^2+3N+1)s^2+(6N+6)ds+6d^2\right]. \tag{13}$$

Since F_x does not contribute to δ_{yp} and F_y does not contribute to δ_{xp}, the total x and y displacements of the probe are given by (2) and (13), respectively. In deriving these equations, we have assumed that the rotation ϕ_i of the beams is sufficiently small so that $\sin(\sum\phi_i)\approx\sum\phi_i$ and $\cos(\sum\phi_i)\approx 1$. This is a reasonably good approximation when $\sum\phi_i \le 0.1$. Therefore, from (8), we have

$$\frac{F_y L}{2EI}N\left((N+1)s+2d\right) \le 0.1. \tag{14}$$

Taking $b=3$ μm, $h=30$ μm, $L=2$ mm, $d=0.3$ mm, $s=33$ μm, and $N=20$, we get $F_y \le 38.4$ nN. Therefore, the force–displacement relation for this configuration is linear only over a limited force range. For larger F_y, the force–displacement relationship becomes coupled (F_y contributes to δ_{xp}), as well as nonlinear. These nonlinearity and cross-coupling are avoided in configuration II as explained in the following.

However, when both F_x and F_y are small, this configuration has some advantages. For example, the sensitivity of this configuration in the x-direction (δ_{xp}/F_x) and in the y-direction (δ_{yp}/F_y) is roughly similar, which is desirable when measuring

both forces at the same time. To summarize, configuration I can measure forces in both x- and y-directions with high resolution but has a limited measurement range.

B. Analysis of Force Sensor Configuration II

In this section, we compute the deflection of the probe (δ_{xp} and δ_{yp}) in configuration II. We adopt the same notations and procedure as we did for configuration I in Section II-A.

1) Probe Deflection Due to F_x: The force F_x on the probe results in a moment $M = -F_x L/2$ and a force F_x at the end in each beam. Therefore, similar to configuration I, the in-plane rotation (ϕ_i) of frame i with respect to frame $i-1$ is equal to zero. Since there is no rotation of the beams, the displacement of frame i with respect to frame $i-1$ is simply the deflection due to bending, which is given by $\delta_{xi} = F_x L^3/24EI$. The deflection of the probe is therefore

$$\delta_{xp} = \sum_{i=1}^{N} \delta_{xi} = \frac{NF_x L^3}{24EI}. \tag{15}$$

Here, N is the number of frames. F_x does not cause any displacement of the beams in the y-direction. Therefore, $\delta_{yp} = 0$.

2) Probe Deflection Due to F_y: The force F_y on the probe results in an axial force F_y and a moment on each frame. As discussed earlier, we neglect the effect of the axial force. From Fig. 2(b), the moment on frame i due to F_y is

$$M_i = F_y\left(2s(N-i) + 3s/2 + d\right). \tag{16}$$

This moment causes a rotation of frame i with respect to frame $i-1$, which is given by

$$\phi_i = \frac{M_i L}{2E(I+I')} \tag{17}$$

where $I' = s^2 bh/4$. Note that $s \approx 10b$, and therefore, $I' \approx 300I$. The moment also leads to bending of the frames, which results in a deflection $M_i L^2/4E(I+I')$. Since $I' \approx 300I$, the rotation and bending of the frame are more than two orders of magnitude smaller than the corresponding rotation (4) and bending $(M_i L^2/2EI)$ of a single beam. As a result, the displacement of the probe (both δ_{xp} and δ_{yp}) due to F_y is negligible. On the other hand, this configuration is still highly sensitive to forces in the x-direction (15), and the relationship between F_x and δ_{xp} remains linear over a large force range (Fig. 9). Hence, this configuration ensures an uncoupled linear force–displacement response and is suitable for cases where only one force component is present or needed to be measured.

III. Out-of-Plane Deflection of the Probe Due to Self-Weight

In most MEMS devices, the effect of gravity is negligible because of their very small size. However, in these force sensors, the torsional stiffness of the beams is very low, and therefore, the rotation of the beams due to self-weight is significant. As a result, there is a fairly large deflection of the probe in the z-direction as shown in the following. For our analysis, we considered configuration II of the force sensor, but the analysis is identical for configuration I.

Each frame in configuration II experiences a torque due to the weight of the frames and the rigid connecting bars in front of it, as well as the probe. The torque on frame i is

$$T_i = \sum_{j=1}^{N-i} 2sjw_f + \sum_{j=1}^{N-i+1} 2s\left(j-\frac{1}{2}\right) w_b + (2s(N-i)+r)\, w_p. \tag{18}$$

Here, w_f is the weight of each frame, w_b is the weight of the rigid bars connecting the frames, and w_p is the weight of the probe. r is the distance in the x-direction of the center of mass of the probe from the middle of the last frame [Fig. 2(b)]. The rotation of frame i with respect to frame $i-1$ is given by $\theta_i = T_i L/2k_\theta$, where $k_\theta = c_1 G b^3 h$ is the torsional stiffness of one beam. G is the shear modulus, and c_1 is a constant that depends on the aspect ratio (h/b) of the beams, with a limiting value of 0.333 as $h/b \to \infty$ [26]. Assuming that θ_i is small, the out-of-plane deflection of frame i with respect to frame $i-1$ is given by

$$\delta_{zi} = 2s\sum_{j=1}^{i-1} \theta_j, \qquad i \geq 2. \tag{19}$$

In (19), the summation is required because the deflection of frame i with respect to frame $i-1$ is proportional to the absolute rotation of frame i. The out-of-plane deflection of the probe is then given by

$$\delta_{zp} = \sum_{i=2}^{N} \delta_{zi} + (d+3s/2)\sum_{i=1}^{N} \theta_i. \tag{20}$$

The first term in (20) is the total deflection of frame N, while the second term is the deflection of the probe with respect to frame N. Using (18) and (19) and $\theta_i = T_i L/2k_\theta$

$$\sum_{i=2}^{N} \delta_{zi} = \frac{s^2 LN(N-1)}{12k_\theta} \times \left[(3N^2+N-2)w_f + (3N^2+5N+2)w_b + (8N-4+6r/s)w_p\right] \tag{21}$$

$$(d+3s/2)\sum_{i=1}^{N} \theta_i = \frac{(d+3s/2)sLN}{12k_\theta} \times \left[(2N^2-2)w_f + (2N^2+3N+1)w_b + (6N-6+6r/s)w_p\right]. \tag{22}$$

As an example, we take $b = 2$ μm, $h = 10$ μm, $L = 2$ mm, $d = 0.4$ mm, $s = 32$ μm, $N = 10$, and the thickness of the probe and the connecting bars t to be 20 μm. $w_f = 2Lbhg\rho_{\text{eff}} + 2sthg\rho_{\text{eff}}$, $w_b = sthg\rho_{\text{eff}}$, and $w_p = L_p thg\rho_{\text{eff}}$. $\rho_{\text{eff}} = \rho_{\text{Si}} - \rho_{\text{water}} = 1330$ kg/m^3 is the effective density of silicon in water, and $L_p = 1.43$ mm is the total length of the probe.

Therefore, $w_f = 1.211$ nN, $w_b = 0.083558$ nN, $w_p = 3.732$ nN, and $r = 112.9$ μm. As mentioned earlier, the torsional stiffness $k_\theta = c_1 G b^3 h$, and for $h/b = 5$, $c_1 = 0.291$ [26]. G depends on the orientation of the force-sensing beams. The beams in our force sensors have their axis along the

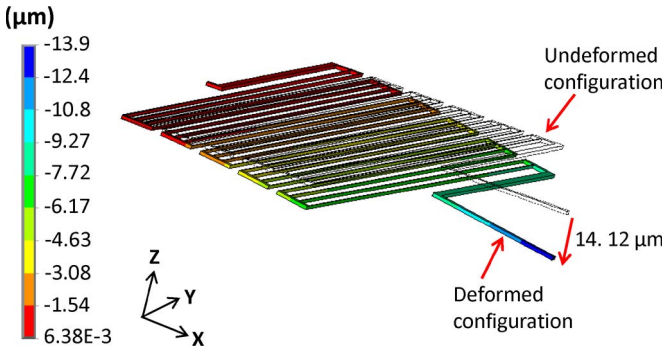

Fig. 3. FE analysis of the out-of-plane deflection of a force sensor in configuration II due to self-weight. The dimensions of the sensor are given in the text. The deflection obtained from the FE analysis (14.12 μm) is very close to the value obtained from theory (14.32 μm). For easier visualization, the deflection of the sensor has been magnified ten times in the figure.

[110]-direction, and the sides of their rectangular cross section are along the [001]- and $[1\bar{1}0]$-directions. For this configuration, $G = 79.6$ GPa [27]. Therefore, $k_\theta = 1.853 \times 10^{-3}$ nN $\cdot$ m^2, and from (20), $\delta_{zp} = 14.32$ μm, which shows that there is a considerable deflection of the probe due to gravity. To verify these results, we calculated the out-of-plane deflection of this sensor due to self-weight by finite-element (FE) analysis (using ANSYS Multiphysics software). The deflection obtained from the FE analysis for this configuration is 14.12 μm (Fig. 3), which is very close to the value obtained from the theoretical analysis.

Apart from the FE analysis, we also experimentally measured the out-of-plane deflection of three different force sensors. The difference between the theoretical prediction and experiments was less than 10% in all three cases. We further verified that the observed deflection is due to gravity and not due to residual stresses in the beams using a simple test. We measured the out-of-plane deflection first with the bottom side of the sensor facing downward and then the top side facing downward. In both cases, the deflection of the beams was downward (along the direction of gravity) and identical in magnitude. If residual stresses were responsible, the direction of the deflection would have reversed, or its magnitude would have been different in the two cases.

Because the displacement of the probe with respect to the reference beam is measured optically, it is desirable to have both the probe and the reference beam in the same z plane. In other words, for ease of measurement, the out-of-plane deflection should be as small as possible. On the other hand, this gravity-induced deflection also confers certain advantages to the force sensor. For example, when the force sensor is immersed into a cell culture environment, the cells are first contacted by the probe because of its lower height. This makes it possible to mechanically manipulate the cells using the probe without interference from other parts of the force sensor.

It is also worth noting that, while the in-plane deflection (δ_{xp}), and hence the force resolution, of the sensor is proportional to N (15), the out-of-plane deflection (δ_{zp}) has an N^4 dependence (21). Therefore, the out-of-plane deflection can be significantly reduced by a small reduction in N, with only a modest reduction in the force resolution. In other words, (15), (21), and (22) provide a basis for optimizing the force resolution and the out-of-plane deflection of the sensor.

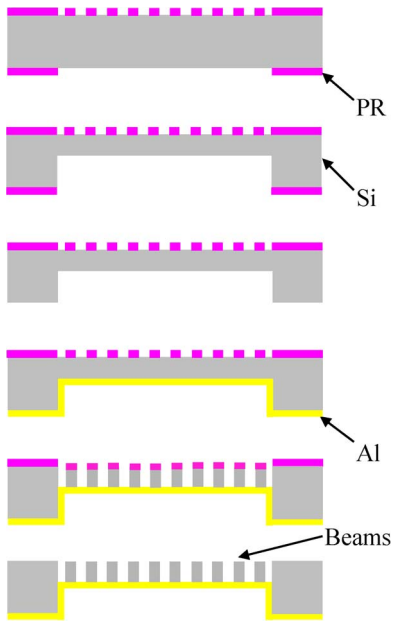

Fig. 4. Schematic of the fabrication process. Note that the beams are connected together by the aluminum film at the end of the process.

IV. Fabrication Process

The force sensors are fabricated using a simple two-mask process shown schematically in Fig. 4. In the first step, a 150-μm-thick (001)-oriented single-crystal silicon wafer is cleaned thoroughly, and a photoresist (AZ-5214) is spun on both sides of the wafer and patterned by photolithography. The top and bottom patterns are identical except that the bottom pattern does not have the force-sensing beams. Then, the wafer is etched from the bottom side using inductively coupled plasma deep reactive ion etching (ICP-DRIE) to the desired depth. The depth of etching controls the depth of the force-sensing beams in the sensor. For example, if the depth of etching is 120 μm, the depth of the beams is $150 - 120 = 30$ μm. After this, the photoresist on the bottom side of the wafer is removed by oxygen plasma, and a thin layer of aluminum (50 nm) is sputter deposited on the bottom side. The wafer is then etched from the top side using ICP-DRIE until the aluminum layer is reached. It is during this step that the force-sensing beams and the other functional features of the force sensor are created. The aluminum layer is deposited primarily for two purposes: 1) to prevent damage to the force-sensing beams during venting in the DRIE process and 2) to avoid damage to the beams from capillary forces when the force sensor is initially immersed into a liquid. In addition, the aluminum layer also facilitates heat transfer during the end of the DRIE step and prevents the structure from heating up [28], [29]. Otherwise, the etch can turn isotropic and destroy the vertical silicon sidewalls. In the last step, the photoresist on the top side is removed by oxygen plasma. Note that, at the end of the fabrication process, the force-sensing beams are still connected together by the aluminum layer.

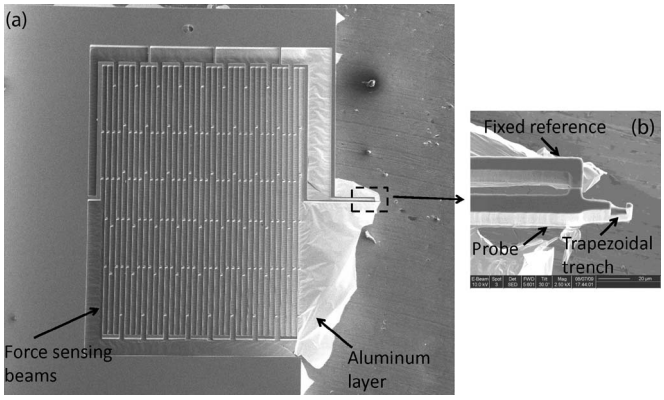

Fig. 5. (a) Scanning electron micrograph of a force sensor with the aluminum film still intact. (b) Magnified view of the probe and the reference beam. A trapezoidal trench was cut into the probe using focused ion beam milling to enable easier gripping of the axons.

V. Scheme for Avoiding Capillary Forces

One of the main problems in MEMS is stiction, which is often encountered during the drying process after the release etch of freestanding components. The meniscus that develops when the wafer is removed from the liquid etchant brings the freestanding components into contact through capillary forces. Once in contact, the components remain stuck together even after the etchant dries out due to various adhesion forces. To avoid stiction-related failures, a number of approaches have been developed [30], [31]. Meniscus formation, for example, can be eliminated through drying techniques such as freeze sublimation or supercritical drying, but these techniques cannot prevent stiction that may occur during device operation. To prevent stiction during both the release etch and device operation, MEMS devices can be coated with antistiction coatings [32].

Capillary forces are also a major constraint in using micromechanical force sensors for biological applications. Since biological studies are usually performed in a liquid environment, the force sensors need to cross the air–liquid interface during their immersion and removal from liquids. Therefore, the force sensors must break the liquid meniscus irrespective of whether they are hydrophilic, hydrophobic, or hydroneutral. Since the force required to break the meniscus is usually very large [33], the force-sensing beams can be irreversibly damaged during this process. Even if the force sensors survive the immersion/removal process, they can suffer stiction-related failures. While antistiction coatings can mitigate stiction-related problems, they limit the scope of biological applications because the sensors often need to be functionalized with proteins such as fibronectin or laminin, and these proteins may not adhere to the antistiction coating. Therefore, to make our force sensors widely applicable for biological studies, we have established a simple scheme to avoid capillary forces.

First, the bottom side of the force sensor, with the aluminum film still intact [Fig. 5(a)], is glued to a 150-μm-thick glass slide (approximately 7 mm wide and 1 cm long). The glass slide with the sensor is then immersed into a beaker containing a diluted solution of AZ 327 metal-ion-free (MIF) developer. During the immersion, the aluminum film protects the beams against damage from capillary forces. Once the sensor is immersed, the developer etches the aluminum film slowly, in the process releasing the flexible beams. In addition, the etching of the aluminum layer exposes the hydrophilic native silicon dioxide layer. Then, the developer is replaced with water by repeated dilution. When the glass slide is removed from the beaker, it retains a droplet of water, thereby keeping the sensor inundated in water, and therefore, the sensor does not experience any capillary forces.

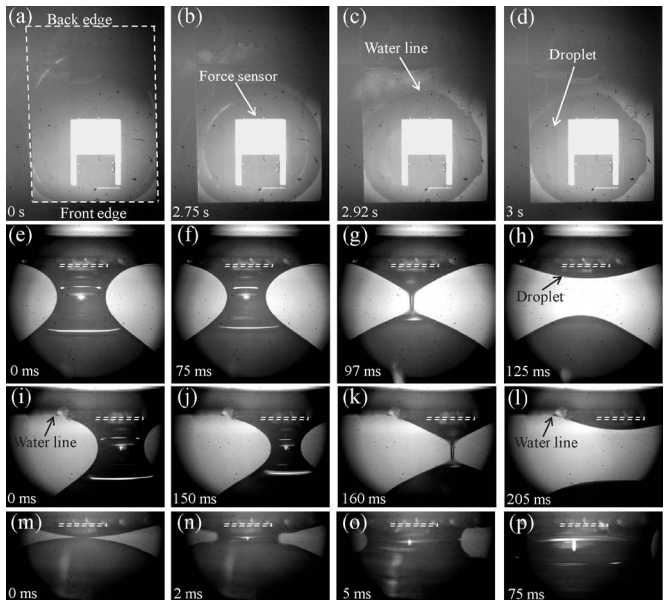

Fig. 6. Sequence of events that occur as the glass slide is removed from and immersed into the water. (a)–(d) View from the top as the glass slide is lifted from the water surface. The water contact line recedes inward as the height becomes larger. (c) shows the configuration just before the droplet pinches off, while (d) shows the droplet after it has separated from the water underneath. The height of the glass slide above the water surface is the same for (c) and (d). The dashed lines in (a) show the edges of the glass slide. (e)–(h) Side view of the meniscus after the onset of instability during the removal from water. The height of the glass slide above the water surface is the same in (e)–(h). The dashed rectangle shows the approximate position of the force sensor. (i)–(l) Side view of the meniscus after the onset of instability showing that the water contact line remains stationary as the droplet pinches off. The height of the glass slide above the water surface is the same in (i)–(l). (m)–(p) Side view of the immersion of the glass slide into the water. (m) shows the droplet on the glass slide just before contact with the water underneath. Note that (a)–(d), (e)–(h), and (i)–(l) are from three different experiments. The movie corresponding to (a)–(d) was recorded at 60 frames per second (fps), while the movies corresponding to (e)–(h), (i)–(l), and (m)–(p) were recorded at 2000 fps. These movies are available as supplementary videos.

To investigate the process through which the glass slide retains the water droplet, we recorded the separation of the glass slide from the water using a high-speed camera. Fig. 6(a)–(d) (top view) shows the sequence of events that occur as the glass slide is lifted up from the water surface. Initially, the water line is pinned along the edges of the glass slide. As the glass slide is lifted up, the water contact line recedes inward into the glass slide until it gets pinned at another location. The pinning occurs because of the heterogeneities in the glass surface, which may arise due to the roughness of the surface or slight variations in surface chemistry. When the glass slide reaches a critical height above the water surface, the meniscus becomes unstable and ruptures. Because the water contact line is pinned on the glass slide, a droplet of water is retained on the slide. Fig. 6(e)–(l) shows the configuration of the meniscus after the onset of the instability. Because of the small size of the force sensor (about

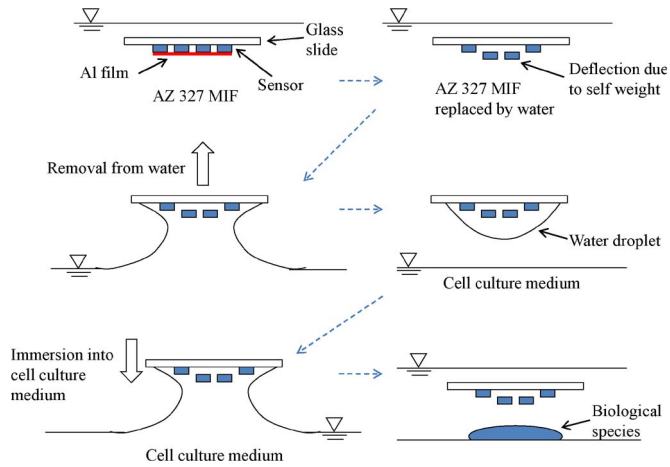

Fig. 7. Schematic of the process by which the force sensor is used for biological studies. Because the glass slide retains a droplet of water, the sensor never experiences any capillary forces. The blue dashed arrows indicate the process flow.

3 mm $\times$ 4 mm), the water droplet that is retained on the glass slide is always sufficient to envelope the sensor. Also, the height of the water droplet is on the order of 1 mm and therefore easily sufficient to keep the sensor, which is only 150 μm thick, inundated.

When the glass slide is being removed from the water, a small forward tilt (less than 5°) is applied so that the droplet is localized in the front region where the force sensor is present. When the glass slide is immersed into another aqueous solution for biological experiments, the solution first contacts the water droplet, keeping the sensor inundated [Fig. 6(m)–(p)]. Therefore, the sensor is not exposed to the capillary forces either during its immersion or removal from water and thus avoids structural damage (we have included the movies corresponding to Fig. 6(a)–(d), (e)–(h), (i)–(l), and (m)–(p) as supplementary material). Apart from water, we have used this technique to conduct biological experiments inside a saline solution, as well as a cell culture medium. We have also functionalized our sensors with fibronectin and poly-L-lysine using this technique. A schematic representation of the steps involved in the application of the force sensors to biological studies, including the process described earlier, is shown in Fig. 7.

VI. Calibration of the Force Sensors

After the force-sensing beams were released, the sensors were calibrated using a tungsten microneedle (N1) of known stiffness. Before calibrating the force sensors, the stiffness of microneedle N1 was obtained using a series of calibrations involving microneedles (N2–N4) with progressively higher stiffness. These tungsten microneedles had lengths ranging from 5 to 10 mm and diameters ranging from 14 to 40 μm. First, microneedle N1 was used to deform microneedle N2, and the ratio of their stiffness was obtained using force balance as

$$k_{\mathrm{N1}}/k_{\mathrm{N2}} = \delta_{\mathrm{N2}}/\delta_{\mathrm{N1}} = q_{12} \tag{23}$$

where k_{N1} and k_{N2} and δ_{N1} and δ_{N2} are the stiffness and deflection of needles N1 and N2, respectively. This procedure

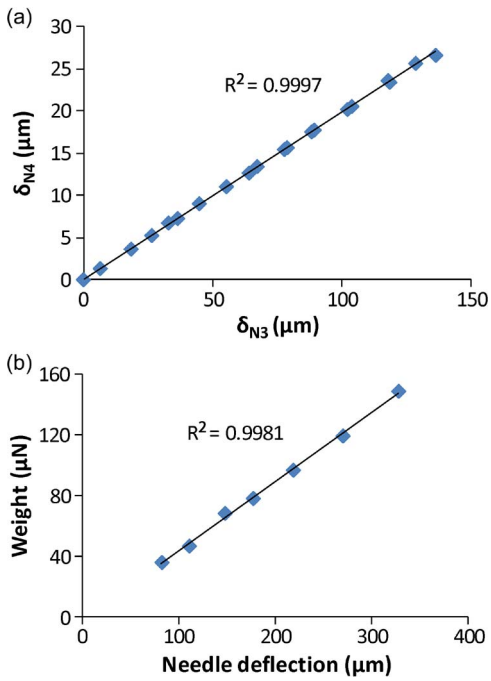

Fig. 8. (a) Calibration of microneedle N3 with needle N4. δ_{N3} and δ_{N4} are the deflections of needles N3 and N4, which are inversely proportional to their stiffness. q_{34} $(k_{\mathrm{N3}}/k_{\mathrm{N4}})$ is given by the slope of the line (0.1982 μm/μm). (b) Direct calibration of needle N4 using weights. The slope of the line (0.4491 μN/μm) gives the stiffness of needle N4.

was then repeated to obtain the ratios (q_{23} and q_{34}) of the stiffness of microneedles N2 and N3 and microneedles N3 and N4. As an example, the calibration of microneedle N3 with N4 is shown in Fig. 8(a). The stiffness of microneedle N4 [Fig. 8(b)] was then directly obtained by hanging weights of known mass from the tip of the needle and measuring the tip displacement. The weights were measured using a mass balance with an accuracy of 10^{-4} g.

Once the stiffness of needle N4 (0.4491 μN/μm) is known, the stiffness of the other needles can be obtained using q_{12}, q_{23}, and q_{34}. For example, $k_{\mathrm{N1}} = q_{12}q_{23}q_{34}k_{\mathrm{N4}} = 1.982$ nN/μm. We note that, since weights are used to directly calibrate needle N4, no assumption/measurement of its mechanical properties (like Young's modulus) is required. The main source of error in measuring the stiffness of needle N4 comes from the weights (an accuracy of 10^{-4} g) since the tip displacement is measured very accurately (error $< 0.1\%$). Because the weights are on the order of 10^{-2} g and multiple weights were used for calibration, the error in the stiffness of needle N4 is within 1%. Because the relative stiffness of the microneedles are known with high accuracy [Fig. 8(a)], the error in the measured stiffness of needle N1 does not exceed 1%.

The stiffness of the force sensors was obtained by calibrating them with needle N1. From the force balance, $F = k_{\mathrm{N1}}\delta_{\mathrm{N1}} = k_{\mathrm{sensor}}\delta_{\mathrm{sensor}}$. k_{N1} is known, and by measuring δ_{N1} and δ_{sensor}, k_{sensor} can be calculated. The force–displacement relationship of two sensors in configuration II is shown in Fig. 9. The stiffness (k_x) of the two sensors obtained from calibration is 0.427 and 4.135 nN/μm, respectively. The calibration also confirmed the linearity of the force response over a large (≈ 150 μm) displacement range. Using image processing techniques (e.g.,

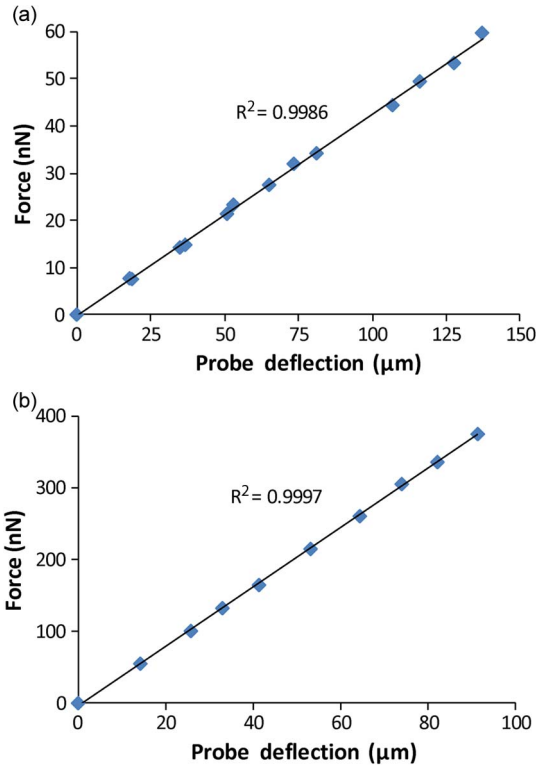

Fig. 9. Force–displacement (F_x versus δ_x) relation of two force sensors in configuration II obtained by calibration with microneedle N1. The stiffness of the two sensors is (a) 0.427 and (b) 4.135 nN/μm, respectively. The figure shows the linearity of the force response of the sensor over a large displacement range.

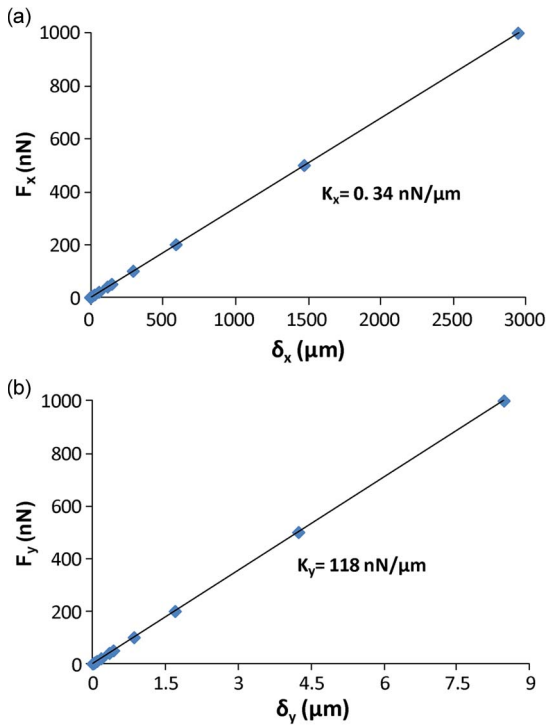

Fig. 10. In-plane deformation of a force sensor obtained from FE analysis. The (a) stiffness of the sensor in the x-direction is approximately 350 times lower than the (b) stiffness in the y-direction. Furthermore, the response remains linear even at a force of 1 μN.

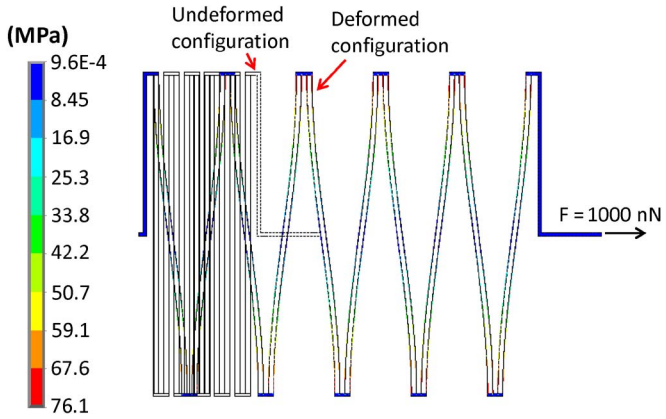

Fig. 11. Stress distribution in the force sensor for $F_x = 1$ μN, obtained using FE analysis. The maximum stress at this high force is still only 76 MPa (see scale bar). The deformation of the sensor has been scaled down to 0.8 times the actual deformation in the figure.

digital image correlation), one can measure displacements with an accuracy of about 100 nm from optical images. Therefore, the force resolution of the stiffer sensor is about 500 pN, and the softer sensor is about 50 pN.

We also performed FE analysis of the in-plane deformation of a force sensor in configuration II (Fig. 10). The dimensions of this sensor are exactly the same as the one in Fig. 3. The stiffness of the sensor along the x-direction (k_x) is 0.34 nN/μm, whereas k_y is 118 nN/μm ($\approx 350k_x$), showing that the sensor is sensitive only to F_x. The results also show that the force-deformation response remains linear even when F_x is 1 μN and δ_x is close to 3 mm. More importantly, the maximum stress in the beams is only 76 MPa (Fig. 11), which is about ten times lower than the failure strength of silicon even after accounting for processing-induced reductions in strength [24]. These results show that our sensors can measure forces ranging from tens of piconewtons to several hundred nanonewtons without failure while retaining linearity.

VII. *In Vivo* Mechanical Response of Axons in *Drosophila*

As mentioned in Section I, mechanical forces influence various cellular processes and functions. Recently, experiments by Siechen *et al.* [34] on *Drosophila* (fruit fly) embryos have revealed an important role for mechanical forces in neuronal function. Their experiments have shown that mechanical tension is necessary for the accumulation of neurotransmitters in the presynaptic terminal of *Drosophila* axons. Vesicle clustering disappears with loss of mechanical tension and is regained upon restoring tension. In addition, an increase in tension enhances the vesicle density at the synapse. Furthermore, they found that the axons maintain a rest tension of about 1 nN and that, when the tension is increased by applying an external force, the axons relax the tension over time. However, the micromechanical sensors that they used had limited resolution (≈ 0.5 nN), which was of similar magnitude to the lowest forces measured.

To understand the mechanics of this tension regulation, we used our force sensors to study the *in vivo* mechanical response

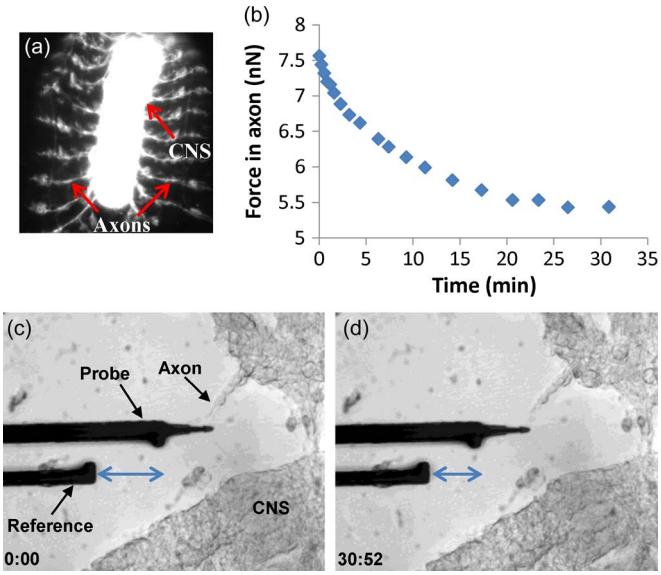

Fig. 12. (a) Fluorescence image of the *Drosophila* embryo nervous system showing the central nervous system (CNS) and axons. (b) Force relaxation in an axon over time. The measurements were made using a force sensor with a stiffness of approximately 0.5 nN/μm. (c) Optical image of the force sensor configuration at the start of the relaxation process. The blue double arrow shows the displacement of the probe with respect to the reference. (d) Force sensor configuration at the end of the relaxation process. Note the reduction in the probe displacement with respect to the reference.

of embryonic *Drosophila* axons. Since these experiments required the measurement of a single force component, the force sensors in configuration II were used. The probes of the force sensors were specially modified for these experiments. Before releasing the beams, a trapezoidal trench was made in the probe [Fig. 5(b)] using focused ion beam milling to enable easy gripping of the axons. The procedure described in Section V was then used to release the force-sensing beams. Finally, the glass slide with the sensor was mounted on a three-axis piezoelectric actuator to apply deformation on the axons.

Drosophila embryos were dissected on a glass substrate inside a saline solution as described in [34]. The force sensor was brought into contact with the axons, and the axons were stretched to a predetermined strain. Then, the relaxation of force in the axon over time was recorded at a fixed force sensor displacement. Fig. 12(b) shows one such force relaxation measurement on an axon. Fig. 12(c) and (d) shows the axon and sensor configuration at the beginning and end of the force relaxation. As evident from Fig. 12, the force in the axons gradually reduces over time and reaches a steady state after about 25 min. Because of the low stiffness (≈ 0.5 nN/μm) and large range of the sensor, we could resolve 50 pN changes in force while being able to measure forces close to 10 nN.

The measurement of forces on the *Drosophila* axons is an example of the application of sensors with low stiffness (< 1 nN/μm). However, our process can also be used to fabricate sensors with much higher stiffness [Fig. 9(b)]. These stiffer sensors would be more appropriate for measuring the response of single cells or agglomeration of cells. For example, they can be used to study the adhesion strength of cells or the response of single cells to large stretches, where the forces can easily exceed 100 nN [35].

VIII. Conclusion

We have designed, fabricated, and calibrated linear high-resolution (50 pN) micromechanical force sensors with a large force measurement range (1 μN). A novel scheme has been established to avoid capillary forces during the immersion and removal of these sensors from aqueous environments to enable their use in biological studies. As a demonstration of their capability and versatility, these force sensors were used to measure subnanonewton forces in *Drosophila* axons subjected to large deformation (50 μm) *in vivo*.

Acknowledgment

The force sensors were fabricated in the Micro and Nanomechanical Systems Cleanroom at the University of Illinois at Urbana–Champaign.

References

[1] G. Bao and S. Suresh, "Cell and molecular mechanics of biological materials," *Nat. Mater.*, vol. 2, no. 11, pp. 715–725, Nov. 2003.
[2] D. Ingber, "Cellular mechanotransduction: Putting all the pieces together again," *FASEB J.*, vol. 20, no. 7, pp. 811–827, May 2006.
[3] N. Wang, J. Butler, and D. Ingber, "Mechanotransduction across the cell surface and through the cytoskeleton," *Science*, vol. 260, no. 5111, pp. 1124–1127, May 1993.
[4] C. Chen, M. Mrksich, S. Huang, G. Whitesides, and D. Ingber, "Geometric control of cell life and death," *Science*, vol. 276, no. 5317, pp. 1425–1428, May 1997.
[5] C. Galbraith and M. Sheetz, "A micromachined device provides a new bend on fibroblast traction forces," *Proc. Nat. Acad. Sci. USA*, vol. 94, no. 17, pp. 9114–9118, Aug. 1997.
[6] S. Suresh, J. Spatz, J. Mills, A. Micoulet, M. Dao, C. Lim, M. Beil, and T. Seufferlein, "Connections between single-cell biomechanics and human disease states: Gastrointestinal cancer and malaria," *Acta Biomater.*, vol. 1, no. 1, pp. 15–30, Jan. 2005.
[7] A. Engler, S. Sen, H. Sweeney, and D. Discher, "Matrix elasticity directs stem cell lineage specification," *Cell*, vol. 126, no. 4, pp. 677–689, Aug. 2006.
[8] K. J. Van Vliet, G. Bao, and S. Suresh, "The biomechanics toolbox: Experimental approaches for living cells and biomolecules," *Acta Mater.*, vol. 51, no. 19, pp. 5881–5905, Nov. 2003.
[9] H. Wang, W. Ip, R. Boissy, and E. Grood, "Cell orientation response to cyclically deformed substrates: Experimental validation of a cell model," *J. Biomech.*, vol. 28, no. 12, pp. 1543–1552, Dec. 1995.
[10] A. Lee, T. Delhaas, L. Waldman, D. Mackenna, F. Villarreal, and A. McCulloch, "An equibiaxial strain system for cultured cells," *Amer. J. Physiol. Cell. Physiol.*, vol. 271, no. 4, pp. C1 400–C1 408, Oct. 1996.
[11] A. Bausch, W. Möller, and E. W. Sackmann, "Measurement of local viscoelasticity and forces in living cells by magnetic tweezers," *Biophys. J.*, vol. 76, no. 1, pp. 573–579, Jan. 1999.
[12] M. Radmacher, "Measuring the elastic properties of living cells by the atomic force microscope," *Methods Cell Biol.*, vol. 68, pp. 67–90, 2002.
[13] J. Guck, J. A. Chiang, and J. Kas, "The optical stretcher: A novel tool to characterize the cytoskeleton," *Mol. Biol. Cell*, vol. 9, p. 609, 1998.
[14] M. Puig-De-Morales, M. Grabulosa, J. Alcaraz, J. Mullol, G. Maksym, J. Fredberg, and D. Navajas, "Measurement of cell microrheology by magnetic twisting cytometry with frequency domain demodulation," *J. Appl. Physiol.*, vol. 91, no. 3, pp. 1152–1159, Sep. 2001.
[15] J. Tan, J. Tien, D. Pirone, D. Gray, K. Bhadriraju, and C. Chen, "Cells lying on a bed of microneedles: An approach to isolate mechanical force," *Proc. Nat. Acad. Sci. USA*, vol. 100, no. 4, pp. 1484–1489, Feb. 2003.
[16] K. Beningo and Y.-L. Wang, "Flexible substrata for the detection of cellular traction forces," *Trends Cell Biol.*, vol. 12, no. 2, pp. 79–84, Feb. 2002.
[17] S.-J. Park, M. B. Goodman, and B. L. Pruitt, "Analysis of nematode mechanics by piezoresistive displacement clamp," *Proc. Nat. Acad. Sci. USA*, vol. 104, no. 44, pp. 17 376–17 381, Oct. 2007.
[18] Y. Sun, K. T. Wan, K. P. Roberts, J. C. Bischof, and B. J. Nelson, "Mechanical property characterization of mouse zona pellucida," *IEEE Trans. Nanobiosci.*, vol. 2, no. 4, pp. 279–286, Dec. 2003.

[19] K. Kim, J. Cheng, Q. Liu, X. Y. Wu, and Y. Sun, "Investigation of mechanical properties of soft hydrogel microcapsules in relation to protein delivery using a MEMS force sensor," *J. Biomed. Mater. Res.—Part A*, vol. 92, no. 1, pp. 103–113, Jan. 2010.
[20] F. Silver, *Biological Materials: Structure, Mechanical Properties, and Modeling of Soft Tissues*. New York: New York Univ. Press, 1987.
[21] B. Pfister, T. Weihs, M. Betenbaugh, and G. Bao, "An *in vitro* uniaxial stretch model for axonal injury," *Ann. Biomed. Eng.*, vol. 31, no. 5, pp. 589–598, May 2003.
[22] S. Yang and T. Saif, "Micromachined force sensors for the study of cell mechanics," *Rev. Sci. Instrum.*, vol. 76, no. 4, pp. 1–8, Apr. 2005.
[23] S. Yang and M. Saif, "MEMS based force sensors for the study of indentation response of single living cells," *Sens. Actuators A, Phys.*, vol. 135, no. 1, pp. 16–22, Mar. 2007.
[24] T. Yi, L. Li, and C. J. Kim, "Microscale material testing of single crystalline silicon: Process effects on surface morphology and tensile strength," *Sens. Actuators A, Phys.*, vol. 83, no. 1–3, pp. 172–178, May 2000.
[25] T. Namazu, Y. Isono, and T. Tanaka, "Evaluation of size effect on mechanical properties of single crystal silicon by nanoscale bending test using AFM," *J. Microelectromech. Syst.*, vol. 9, no. 4, pp. 450–459, Dec. 2000.
[26] S. Timoshenko, *Theory of Elasticity*. New York: McGraw-Hill, 1970.
[27] J. J. Wortman and R. A. Evans, "Young's modulus, shear modulus, and Poisson's ratio in silicon and germanium," *J. Appl. Phys.*, vol. 36, no. 1, pp. 153–156, Jan. 1965.
[28] S. E. Alper, A. Aydemir, and T. Akin, "Stepped-etching for preserving critical dimensions in through-wafer deep reactive ion etching of thick silicon," in *Proc. Int. Conf. Solid-State Sens., Actuators, Microsystem, Transducers*, Denver, CO, Jun. 2009, vol. 1110–1113.
[29] P. J. Gilgunn and G. K. Fedder, "On the origin of selectivity and anisotropy loss during microstructure release etch," *J. Micromech. Microeng.*, vol. 20, no. 3, p. 035 021, Mar. 2010.
[30] W. M. Van Spengen, "MEMS reliability from a failure mechanisms perspective," *Microelectron. Reliab.*, vol. 43, no. 7, pp. 1049–1060, Jul. 2003.
[31] B. Bhushan, "Adhesion and stiction: Mechanisms, measurement techniques, and methods for reduction," *J. Vac. Sci. Technol. B, Microelectron. Nanometer Struct.*, vol. 21, no. 6, pp. 2262–2296, Nov. 2003.
[32] B. H. Kim, T. D. Chung, C. H. Oh, and K. Chun, "A new organic modifier for anti-stiction," *J. Microelectromech. Syst.*, vol. 10, no. 1, pp. 33–40, Mar. 2001.
[33] T. A. Saif, "On the capillary interaction between solid plates forming menisci on the surface of a liquid," *J. Fluid Mech.*, vol. 473, no. 1, pp. 321–347, 2002.
[34] S. Siechen, S. Yang, A. Chiba, and T. Saif, "Mechanical tension contributes to clustering of neurotransmitter vesicles at presynaptic terminals," *Proc. Nat. Acad. Sci. USA*, vol. 106, no. 31, pp. 12 611–12 616, Aug. 2009.
[35] S. Yang and T. Saif, "Reversible and repeatable linear local cell force response under large stretches," *Exp. Cell Res.*, vol. 305, no. 1, pp. 42–50, Apr. 2005.

Jagannathan Rajagopalan received the B.Tech. and M.Tech. degrees in mechanical engineering from the Indian Institute of Technology Madras, Chennai, India, in 2004, and the Ph.D. degree in mechanical engineering from the University of Illinois at Urbana–Champaign, Urbana, in 2009.

He is currently a Postdoctoral Research Associate in the Department of Mechanical Science and Engineering, University of Illinois at Urbana–Champaign. His research interests include the mechanics of thin films, nanoscale material behavior, BioMEMS, and the mechanics of biological systems.

Alireza Tofangchi received the B.S. degree in mechanical engineering from Shiraz University, Shiraz, Iran, in 1993, and the M.S. degree in applied mechanics from Sharif University of Technology, Tehran, Iran, in 1996. He is currently working toward the Ph.D. degree at the University of Illinois at Urbana–Champaign, Urbana, in Prof. Saif's group.

He was a Lecturer in the Department of Mechanical Engineering, Razi University, Kermanshah, Iran, from 1996 to 2004, and in the Department of Engineering Mechanics, University of Nebraska, Lincoln, from 2005 to 2007. His current area of research is cell mechanics, particularly *in vivo* mechanosensitivity of *Drosophila* neurons.

M. Taher A. Saif received the B.S. degree in structural civil engineering from the Bangladesh University of Engineering and Technology, Dhaka, Bangladesh, in 1984, the M.S. degree in structural civil engineering from Washington State University, Pullman, in 1987, and the Ph.D. degree in theoretical and applied mechanics from Cornell University, Ithaca, NY, in 1993.

From 1993 to 1997, he was a Postdoctoral Associate in the Electrical Engineering Department, Cornell University. He is currently the Gutgsell Professor in the Department of Mechanical Science and Engineering, University of Illinois at Urbana–Champaign, Urbana. His research focuses on the mechanics of MEMS, submicrometer material behavior, BioMEMS, and the mechanics of single living cells such as neurons and cardiac cells.